Wind and Structures, *Vol. 27, No. 1 (2018) 29-40*
DOI: https://doi.org/10.12989/was.2018.27.1.029

Numerical analysis of wind field induced by moving train on HSR bridge subjected to crosswind

Yujing Wang*[1], He Xia[1,2], Weiwei Guo[1,2], Nan Zhang[1,2] and Shaoqin Wang[3]

[1]*School of Civil Engineering, Beijing Jiaotong University, Beijing 100044, China*
[2]*Beijing Key Laboratory of Structural Wind Engineering and Urban Wind Environment, Beijing 100044, China*
[3]*School of Science, Beijing University of Civil Engineering and Architecture, Beijing 100044, China*

(Received March 25, 2017, Revised December 10, 2017, Accepted March 23, 2018)

Abstract. To investigate the characteristics of the combined wind field produced by the natural wind field and the train-induced wind field on the bridge, the aerodynamic models of train and bridge are established and the overset mesh technology is applied to simulate the movement of high-speed train. Based on ten study cases with various crosswind velocities of 0~20 m/s and train speeds of 200~350 km/h, the distributions of combined wind velocities at monitoring points around the train and the pressure on the car-body surface are analyzed. Meanwhile, the difference between the train-induced wind fields calculated by static train model and moving train model is compared. The results show that under non-crosswind condition, the train-induced wind velocity increases with the train speed while decreases with the distance to the train. Under the crosswind, the combined wind velocity is mainly controlled by the crosswind, and slightly increases with the train speed. In the combined wind field, the peak pressure zone on the headstock surface moves from the nose area to the windward side with the increase of wind velocity. The moving train model is more applicable in analyzing the train induced wind field.

Keywords: high-speed train; train-induced wind; crosswind; combined wind field; numerical analysis; overset mesh

1. Introduction

With the rapid development of high-speed railway (HSR) in China, the aerodynamic load brings a series of new challenges to the running safety, stability and comfort of high-speed trains, which is one of the practical engineering issues that should be urgently resolved. When a train runs at high speed, a complex air stream occurs around the train-body, and this kind of air flow is called the train-induced wind. In the natural environment, the combined action of the train-induced wind and the crosswind makes the flow field around the train-bridge system more complex. It is important to study the aerodynamic interaction among the wind loads, train and bridge in this combined wind filed, so as to ensure the safety and normal operation of the bridge and the high-speed train.

There have been many researches about the wind loads on bridges and train vehicles, and have achieved some results (Wang and Xu 2015, Zhai *et al.* 2015, Cai *et al.* 2015). The buffeting wind loads on vehicles are usually obtained through the combination of the crosswind velocity and the running train speed. When a train runs at a high speed under crosswind, there exists an aerodynamic interference effect between the bridge at rest and the train in moving. Ashamed *et al.* (1985) studied the aerodynamic characteristics of road and rail vehicles (including maglev vehicles) based on theoretical and experimental methods. Xu *et al.* (2007) and Guo *et al*. (2007) investigated the dynamic response of a suspension bridge to typhoon and moving trains. Guo *et al.* (2015) analyzed the running safety of high-speed train on HSR bridge under cross wind and the aerodynamic effect of wind barriers. Zhang *et al.* (2015) discussed the shielding effect of bridge tower with triangular wind barriers under cross wind, based on the coupled wind-train-bridge system model. Chen *et al.* (2011) presented a framework for dynamic stress analysis of long suspension bridges under wind, railway and roadway loads. Zhang *et al.* (2013) analyzed the windbreak effect of barriers with different heights and porosities for the train-bridge system subjected to cross wind. In order to solve the aerodynamic problems of high-speed railway, the scholars have done extensive studies and achieved some results. Li *et al.* (2014) fully considered the aerodynamic interaction effects between a moving train and a bridge deck, but the movement of the train was realized by the relative motion theory.

There have been many researches about simulation of moving trains. The aerodynamic characteristics of train-bridge system are usually obtained via numerical simulations and wind tunnel tests. The aerodynamic forces on vehicles in previous studies were mainly calculated based on the work of Baker (2002) or obtained from wind-tunnel tests. Premoli *et al*. (2016) compared the steady and moving railway vehicles under cross wind by using CFD software. Avadiar *et al.* (2016) investigated the effect of train composition length on wake structures, using the POD and DMD decomposition methods (2016). Asress *et al.* (2014) simulated the flow of turbulent crosswind over an ICE2 high-speed train model in the case scenarios of static ground and moving ground for different yaw angles. Huang *et al.* (2016) adopted the improved delayed detached eddy

*Corresponding author, Ph.D.
E-mail: qearjing@163.com

ISSN: 1226-6116 (Print), 1598-6225 (Online)

simulation (IDDES) approach to calculate the slipstream of a 1/25-scale four-coach model and obtained the safe standing distance. Hemida *et al*. (2014) studied the slipstream and wake flow of a 1/20 scale model of a shape-simplified ICE2 train. The results showed that the maximum of slipstream velocity appeared at the streamlined head region and the near wake flow region of the train. Yao et al. (2013) studied the wake flow of high-speed trains marked by the federation and collapse of numerous vortices by adopting URANS and DES. Krajnovic *et al*. (2012) took the large eddy simulation method to analyze the flow around the simplified moving train model under a crosswind. Rezvani *et al*. (2014) investigated the airflow passing the ATM train under different yawing conditions and the unsteady aerodynamic performance of crosswind stability by numerical simulation.

However, in most previous researches, the Relative Movement Theory was used in simulating the moving train, which was not consistent with the actual train motion. In this paper, the combined effects of train-induced wind flow and crosswind flow around the train-bridge system are analyzed based on the Computational Fluid Dynamics (CFD). The aerodynamic model of train-bridge system is established, which consists of a box girder and a simplified CRH2 high-speed train composed of a head-car, a middle-car and a tail-car. Based on the three-dimensional Reynolds-averaged Naiver-Stokes equation of incompressible viscosity fluid and the k-ε turbulence model, the turbulent flow around the CRH2 train running at 200~350 km/h on a HSR bridge subjected to crosswind of 0~20 m/s was analyzed using the finite volume method, to obtain the pressure and velocity distributions of slipstream around the train. In addition, the influence of running train and crosswind on the combined flow field is studied. Finally, the train-induced wind fields produced by the static train model and the moving train model are compared.

2. Numerical model

2.1 Governing equations

The equations governing the flow around the train-bridge system are the continuum and momentum equations, which take the following tensor forms:

The continuum equation

$$\mathrm{div}\vec{u} = 0 \tag{1}$$

The momentum equation

$$\mathrm{div}(u\vec{u}) = -\frac{1}{\rho}\frac{\partial p}{\partial x} + \upsilon \mathrm{div}(\mathrm{grad}u) \tag{2}$$

$$\mathrm{div}(v\vec{u}) = -\frac{1}{\rho}\frac{\partial p}{\partial y} + \upsilon \mathrm{div}(\mathrm{grad}v) \tag{3}$$

$$\mathrm{div}(w\vec{u}) = -\frac{1}{\rho}\frac{\partial p}{\partial z} + \upsilon \mathrm{div}(\mathrm{grad}w) \tag{4}$$

where, $\vec{u}$ is the velocity in the coordinate system; u, v and w are the speed components in x, y and z directions, respectively; is the density, and p is the air pressure of the fluid; υ is the kinetic viscosity of the air.

2.2 Geometry model

The CRH2 EMU (electronic multiple units) is taken as the analysis object, which is a type of high-speed trains adopted in HSR lines in China. The train model is shown in Fig. 1.

In the model, the train is simplified as geometry with smooth curved surfaces, by properly ignoring the detailed characteristics such as the car lights, doorknobs, bogies and pantographs. Because the real train is a slim-lined object, if the flow field for the whole train is to be simulated, it requires a fast calculation speed and high memory capacity for the computer, resulting in massive computational work. Therefore, considering the cross-section of the train keeps unchanged at its middle part, where the variation of aerodynamic force tends to be stable, the train model is only composed of a head-car, a middle-car and a tail-car, and the head-car and the tail-car have the same dimensions. The headstock is a complicated three-dimensional curved surface with the length of 9.5 m. The tip of the nose is 0.94 m above the rail surface. The car-body is 3.38 m in width and 3.7 m in height. The length of the head-car and the tail-car is 25.7 m, and that of the middle-car is 25 m, so the total length of the train model is 76.4 m.

The bridge considered is a 32m-span simply-supported beam bridge adopted on the Lanzhou-Xinjiang HSR line. The bridge model is simplified as a 300 m-long continuous beam with a solid section, without considering the piers. The profile of the beam is retained as its original shape, whose height and width are respectively 2.85 m and 12.2 m. The details of the handrails, rails, track beds and sleepers are neglected, while remains a 0.2 m interspace between the train bottom and the deck surface to simulate the track structure. The center-to-center distance between two tracks is 5 m, and the train model runs on the track at the windward side.

2.3 Aerodynamic model

Illustrated in Fig. 2 is the configuration of the computational domain, where the length L, width B and height H are 300 m, 220 m and 75 m, respectively. The bridge is extended through the whole computational domain. The train model runs along the X direction, and the nose of the head-car is 201.8 m to the front boundary (Wall 1) of the computational domain when it begins to move. To let the turbulent flow fully develop, several calculation regions are repeatedly tried and the following one is chosen: center line of the bridge is 40 m above the ground, 60 m away from the Inlet and 160 m to the Outlet. The train-bridge system is established as the same scale of the model in numerical simulation.

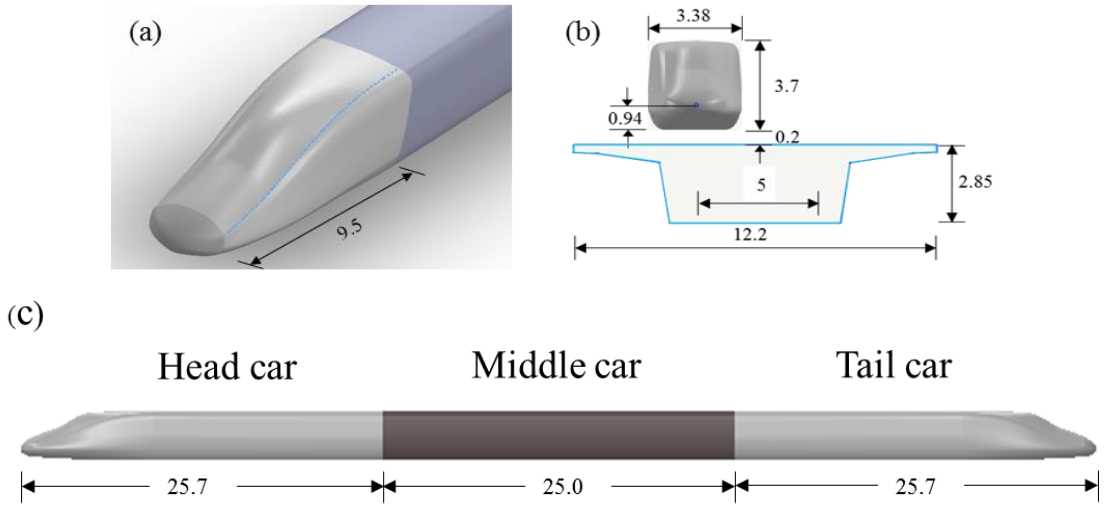

Fig. 1 Geometry and dimensions of the train model (unit: m)

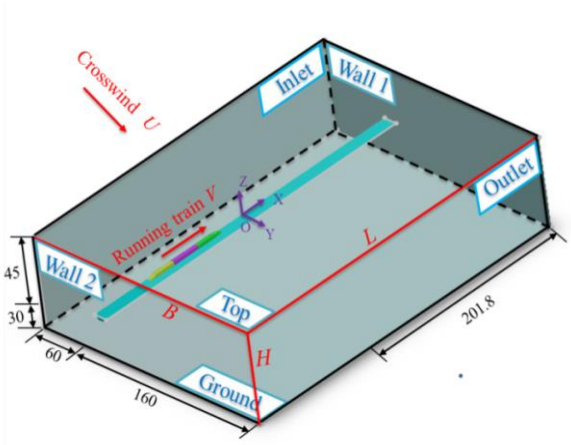

Fig. 2 Computational domain and boundary conditions (unit: m)

The boundary conditions include:

(1) Inlet: velocity-inlet with mean wind
(2) Outlet: pressure-outlet with zero static pressure
(3) Ground, front boundary Wall 1 and rear boundary Wall 2: non-slip wall
(4) Top: slip wall
(5) Surface of train: non-slip wall
(6) Surface of bridge: non-slip wall

Because the crosswind velocity is very small (Mach number is far less than 0.3), the train-induced wind flow and the crosswind flow around train-bridge system can be handled as an incompressible stationary flow problem. The iteration method of successive lower relaxation is adopted to calculate the wind pressure and wind velocity, whose relaxing factor should be as large as possible to accelerate the convergence, but a too large relaxing factor may lead to the instability of computational process and the divergence of solution. Because the SIMPLE Algorithm can select a biggest relaxing factor which has a better stability, it is employed to couple the pressure with the velocity field and to modify the pressure with the iteration method. The k-two-equation model is used for the turbulence model, which can better deal with the flow problem of large streamline bending via updating the turbulent viscosity. The pressure-based implicit solution algorithm is employed.

In the case study, the crosswind velocity is perpendicular to the train moving direction, the wind velocity is chosen as 0 m/s, 10 m/s, 15 m/s and 20 m/s, and the train speed is set to be 200 km/h, 250 km/h, 300 km/h and 350 km/h, respectively. So the Reynolds number varies from 2,532,000 to 5,065,000, approximately.

The computational accuracy and efficiency of numerical simulation is directly related to the quality and quantity of FE meshing. To simulate the complicated three-dimensional surface of headstock and tailstock, the maximum mesh size of car-body surface is set as 0.2 m and the minimum size is 0.1 m. The maximum mesh size of bridge surface is 0.3 m and the minimum size is 0.05 m. The maximum mesh size of computational domain boundary is 1.0 m and the minimum size is 0.5 m. Considering the complex boundary layer turbulence, where the turbulence development is difficult to catch, the boundary layer mesh around the car-body is taken as 0.008 m, and that around the bridge is 0.01 m. The refined meshes are employed for three special local regions, as shown in Fig. 3: gap region A between the train and bridge, region B around the train, and region C around the train-bridge system. The three regions are partially overlapped, where the meshes adopt smaller sizes between two or the smallest among three of them. The dimensions of region A is 3.4 m (wide) × 0.2 m (high), region B is 14 m × 6.5 m, and region C is 33 m × 16 m. The refined mesh sizes of region A, B and C are 0.1 m, 0.4 m and 0.8 m, respectively. In the other regions, the structured hexahedral meshes are adopted to accelerate the computation speed and convergence rate. In the region far away from the train-bridge system, the mesh gradually becomes less dense. The total quantity of mesh is about 7,500,000.

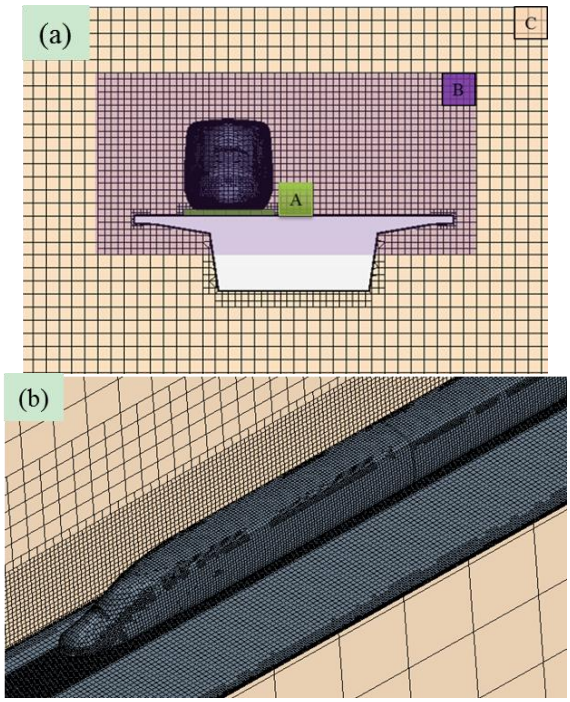

Fig. 3 Meshes of train-bridge system at different perspectives

2.4 Realization of moving train

The overset mesh method is adopted to simulate the movement of high-speed train. In this method, the complicated flow region is divided into several sub-regions with simple geometric boundaries. In the sub-regions, the computational meshes are independently generated, among which exist covering, nesting or overlapping relationship. The flow information is matched and coupled through interpolation at the boundary of the overlapped sub-regions, to transmit the boundary information for the flow field calculation among the sub-regions. As shown in Fig. 4, the whole calculation region is divided into two sub-regions: the train moving sub-region (slave region) and the static calculation sub-region (control region), which are separated by the geometry interface Face 1. The control region contains the bridge model and the computational domain boundaries, while the slave region contains the train model.

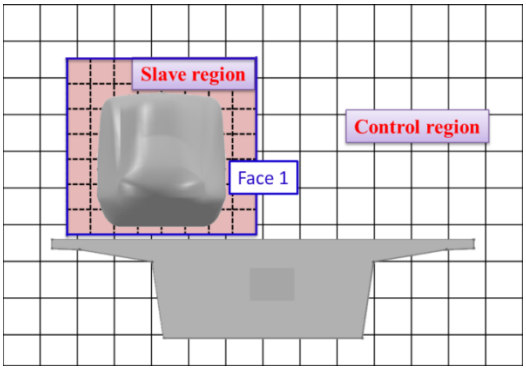

Fig. 4 Principle of the overset mesh method (unit: m)

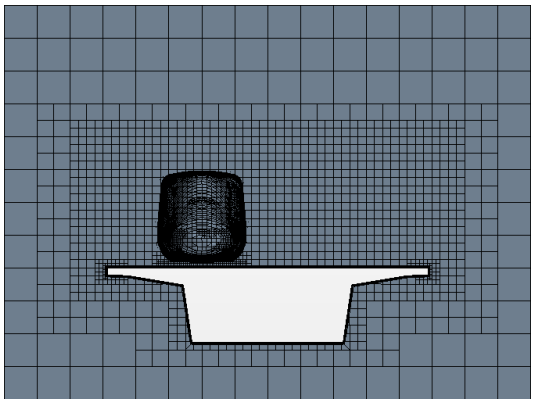

(a) coarse mesh

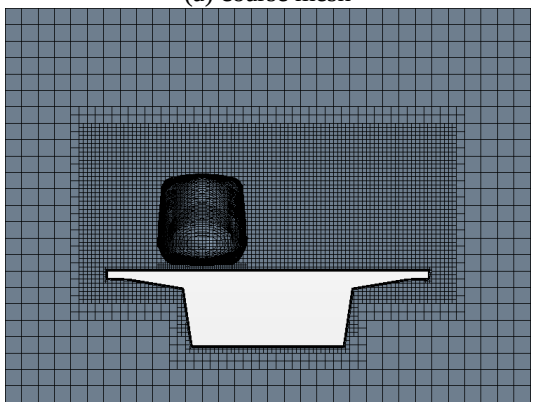

(b) refined mesh

Fig. 5 Volume mesh of different types

To ensure the train running in the fully-developed flow field, the flow field around the static train is calculated before the train moves until it is fully developed. When the train moves to a certain positon, the overlapping mesh of the control region and the slave region is calculated via linear interpolation, to obtain the wind field around the subject structures at the moment. When the calculation at the position is converged, the train moves to the next position, and the next calculation is performed, until the train stops moving. The physical time interval in the numerical calculation is set to be 0.001 s to minutely capture the formation and evolution of vortices in every step.

2.5 Verification of models

To verify the accuracy of mesh and turbulence model in the paper, a 3-D full-scaled geometry model of train-bridge system with same CRH2 train in the reference (Guo *et al*. 2014) is established. In order to further explore the optimal mesh, two sets of mesh, a coarse mesh and a refined mesh, are applied. The coarse mesh mentioned above contains about 7,500,000 cells and the refined mesh contains about 11,000,000 cells. Fig. 5 shows the volume mesh of them.

Two simulations with different meshes are conducted with the same boundary layer and parameters setting, and the tri-component coefficients of the middle-car are compared with the experimental results, as illustrated in Table 1.

Table 1 Tri-component coefficients of middle-car

Middle-car		C_D	C_L	C_M
Test		1.335	-0.480	0.207
Simulation	Coarse mesh	1.260	-0.370	0.298
	Refined mesh	1.263	-0.373	0.290

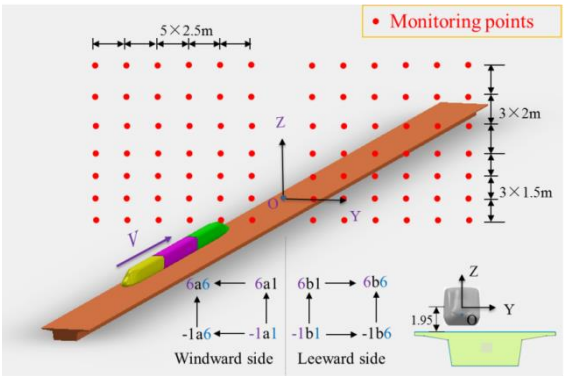

Fig. 6 Layout of monitoring point arrangement (unit: m)

Table 1 shows that the simulated results have a good agreement with the experimental ones, indicating a high accuracy of simulation. Furthermore, the coarse mesh is more suitable after considering the simulation accuracy and computation speed, comprehensively.

3. Monitoring configuration

When a train runs at high speed, it drives the surrounding air to flow, producing the train-induced wind field. Under crosswind, the train-induced wind field and the crosswind field constitute a complicated combined wind field. To study the train-induced wind field, the combined wind field and their influence range, 84 monitoring points (-1a6~6a6 and -1b1~6b6) are set up at the monitoring section over the bridge, whose arrangement is shown in Fig. 6. When the train passes the monitoring section, the flow field information can be captured by the monitoring points.

As is shown in Fig. 6, the monitoring section is placed above the bridge at the center of the computational domain, perpendicular to the longitudinal axis of the bridge, and the coordinate origin of the monitoring section is located at the cross centroid of the train, 1.95 m above the bridge deck. Since the distance between the centers of two tracks is 5 m, in transverse direction, the monitoring points on both sides of the train are symmetric about the Z-axle, ranging from -15 m to 15 m. There are 6 columns of monitoring points at the locations of Y=±2.5 m, ±5 m, ±7.5 m, ±10 m, ±12.5 m and ±15 m, arranged on both sides of the train. In vertical direction, monitoring points are arranged from -1.5 m to 9 m. There are 6 rows of monitoring points arranged with unequal spaces to reduce the calculation work: 4 rows at Z=-1.5 m, 0 m, 1.5 m and 3 m from the cross centroid of the train, numbering as -1a~3a and -1b~3b, and 3 rows at Z=5 m, 7 m and 9 m, numbered as 4a~6a and 4b~6b, respectively. This ensures that the wind velocity at the same height of vehicle roof, vehicle center and vehicle boot can be detected.

4. Result analysis

Train-induced wind field is the air flow caused by the train movement, and it combines with the crosswind field to form the combined wind field. Wind velocity and wind pressure are two important indexes, which are taken to evaluate the characteristics of train-induced wind field as well as the combined wind field.

4.1 Train-induced wind field without crosswind influence

When a train runs on the bridge without influence of crosswind, the air close to the train flows sharply, causing complex flows around the train and the bridge. Because the bridge does not move, it has little influence on the air flow, the train-induced wind velocity U_T is primarily affected by the train speed V.

4.1.1 Distribution of train-induced wind velocity in the monitoring section

For better comparison, in the analyses hereinafter, the no-dimensional parameters $\eta_W=|Y/B_T|$, $\eta_L=Y/B_T$ and $\zeta=Z/H_T$ are used to indicate the monitoring points, where η_W and η_L are the relative transverse distances of the windward side and the leeward side, and ζ is the relative vertical distance, of monitoring points from the train centroid, B_T (3.38 m) and H_T (3.7 m) are the width and height of the train, respectively. When the subscripts W and L of η are omitted, it means that the η represents both sides of the train.

When the train passes through the monitoring section, the pressure at the monitoring points will change. Shown in Fig. 7 are the time histories of wind pressure at monitoring points 1a1~1a6 and -1a1~6a1 under the condition of non-crosswind and 200 km/h train speed.

As can be seen, the wind pressures at all monitoring points change similarly with time: when the headstock passes through the monitoring section, the pressures rapidly increase to the wave peaks, and then decrease to the wave troughs. When the train body passes the monitoring section at a constant speed, the pressures keep relatively stable, basically unchanged. Then, when the tailstock passes the monitoring section, the pressure first decreases to the wave troughs and then increases to wave peaks. The wave peaks and the wave troughs induced by the tailstock are different with those by the headstock. When the train runs away from the monitoring section, the pressure gradually reduces to zero, and becomes stable slowly.

As shown in Fig. 7(a), the amplitudes of wind pressure vary along the transverse direction: at the cross centroid height of the train (ζ =0), for point 1a1 (2.5 m from the centroid, η_W =0.74), the pressure has a wave peak of 147 Pa and a wave trough of -159 Pa; while for point 1a2 (5 m

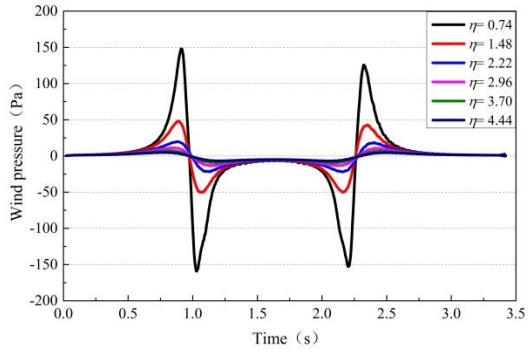

(a) at different transverse locations

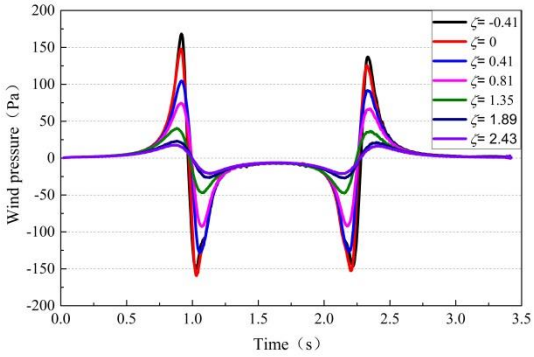

(b) at different heights

Fig. 7 Time histories of wind pressure at various monitoring points

from the centroid, η_W =1.48), the pressure has the wave peak of 48 Pa and the wave trough of -50 Pa, respectively decreased by 67.3% and 68.5%. Beyond the relative distance of 5 m (η_W =1.48), the pressure continues to decrease until 5 Pa at point 1a6 (15 m from the train centroid, η_W =4.44).

As shown in Fig. 7(b), the amplitudes of wind pressure are different at various heights: among the monitoring point column -1a1~6a1 (η_W =0.74, ζ =-0.41~2.43), the maximum wave peak is 168Pa and the maximum wave trough is -150 Pa, both appearing at point –1a1 (η_W =0.74, ζ =-0.41) which is 1.5 m below the centroid.

Fig. 8 shows the transverse component U_{TY} and vertical component U_{TZ} of train-induced wind velocity under the condition of non-crosswind and train speed 200 km/h, in which the abscissa denotes the relative position of monitoring points. When without crosswind, the wind fields on both sides of the train are basically symmetric, so only the wind velocity on the left side is provided in the figure.

It can be seen from Fig. 8(a) that, U_{TY} at the nearest location of the train (2.5 m, η_W=0.74) is the largest, which is 5.8 m/s, appearing at the height of Z=0 m. U_{TY} decreases with the distance from the train, and it becomes less than 0.5 m/s at 10 m (η_W =2.96); for the same transverse distance, the higher the monitoring point, the smaller the amplitude of U_{TY}. From Fig. 8(b), one can find that U_{TZ} at the nearest location of the train (2.5 m, η_W=0.74) is the largest, which is 2.4 m/s, appearing at the height of 1.5 m (ζ =0.41) and 3.0 m (ζ =0.81); in general, the farther the monitoring point from the car-body, the smaller the amplitude of U_{TZ}. For the monitoring point -1b1 (η_L =0.74, ζ =-0.41), since it is close to the deck, the vertical development of flow field is blocked, the vertical component of train-induced wind velocity is small.

With the increase of transverse distance from the car-body, both U_{TY} and U_{TZ} decrease rapidly, which become less than 0.2 m/s at the location of 10 m (η_W=2.96). It can be seen that the influence of train-induced wind can be neglected basically when the distance is larger than 10 m.

4.1.2 Variation of train-induced wind velocity vs train speed

To study the variation of wind velocity components U_{TY} and U_{TZ} versus train speed, four cases of train speeds at 200 km/h, 250 km/h, 300 km/h and 350 km/h without considering crosswind are analyzed.

Shown in Fig. 9 are the time histories of U_{TY} and U_{TZ} at point 1a1 (η_W =0.74, ζ=0) when the train passes at four speeds, and in Fig. 10 are the equi-velocity contours of train induced wind field component U_{TY} and U_{TZ}.

It can be seen from Fig. 9 that both the U_{TY} and U_{TZ} amplitudes increase with the train speed. When the train speed is 350 km/h, the positive peak of U_{TY} is 10.1 m/s and the negative is -10.7 m/s. In the time history of U_{TY}, the negative value appears first and then the positive value. It is due to the 'push out' effect of headstock on the air flow, which makes the flow diverse to two sides of the headstock and moves outward from the monitoring points.

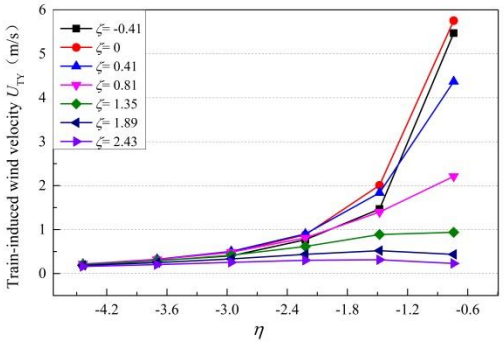

(a) U_{TY}

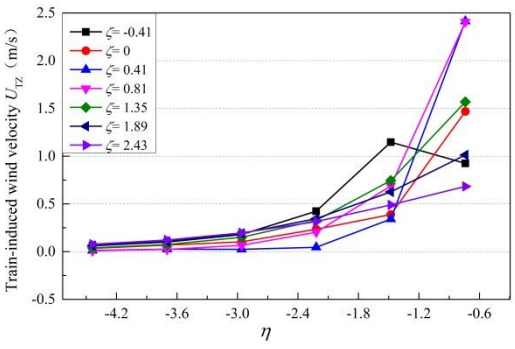

(b) U_{TZ}

Fig. 8 Transverse and vertical components of train-induced wind velocity

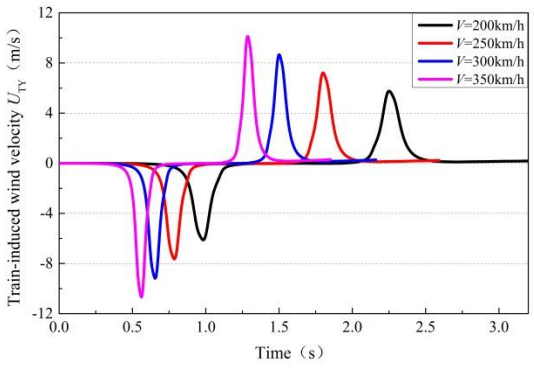

(a) U_{TY}

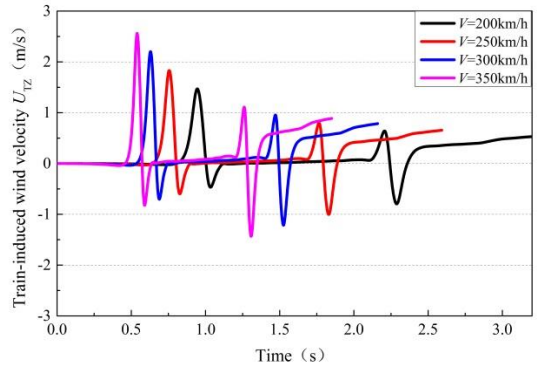

(b) U_{TZ}

Fig. 9 Train-induced wind time histories of point 1a1 vs train speed

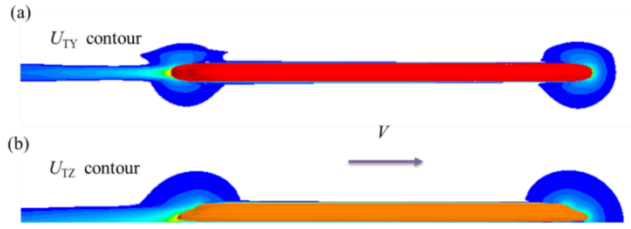

Fig. 10 Equi-velocity contours of train induced wind field component U_{TY} and U_{TZ}

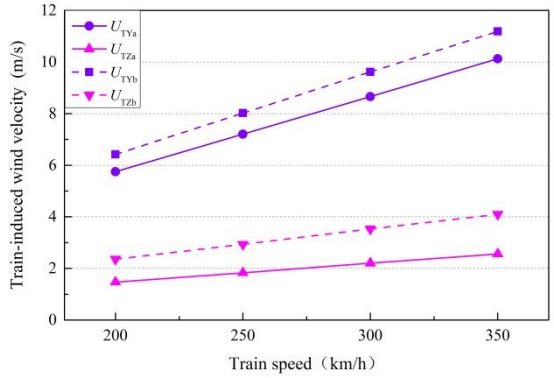

Fig. 11 Distribution of train-induced wind velocity components vs train speed

When the train body passes, the wind field is stable with pliant flow, and U_{TY} is close to zero. When tailstock passes, a 'drag' effect is produced on the air, making the flow inward. Because the train model is symmetric, the U_{TY} induced by tailstock is similar with that by headstock, but the tailstock produces a big air 'tail', as shown in Fig. 10(a), which means the attenuation of U_{TY} induced by tailstock needs more time.

From Fig. 9(b) one can see that under train speed of 350 km/h, the positive peak of U_{TZ} is 2.6 m/s and the negative is -1.43 m/s. The blocking effect of bridge on the vertical development of flow field makes a big difference between the positive and negative amplitudes of U_{TZ} at various train speeds. When the tailstock drives away, the top surface of the gap between train and bridge turns into a free boundary, making the flow upward and accelerate, therefore, U_{TZ} has an increasing tendency, unlike U_{TY} which decays immediately.

Fig. 11 shows the components U_{TY} and U_{TY} of train-induced wind velocity vs train speed at point 1a1 on the left side and point 1b1 on the right side, respectively denoted with subscript a and b. As can be seen from the figure that when train speed varies from 200 km/h to 350 km/h, the transverse components U_{TYa}, U_{TYb} and vertical components U_{TZa}, U_{TZb} of train-induced wind velocity all increase with the train speed. The tendency is almost linear, and the slopes of the four lines from top to bottom are 0.89%, 0.8%, 0.33% and 0.2% respectively. Therefore, the transverse component of wind velocity changes faster with train speed than the vertical component, whether on the left side or on the right side. When the train runs on one track, the train-bridge system model is not exactly symmetrical about the XOZ plane, there is a difference between the wind fields on both sides of the train, but from Fig. 11 one can see that the difference is small, so it is practicable to study the wind field on one side.

4.2 Train-induced wind field with crosswind influence

Under crosswind, the train produces a squeezing action on the crosswind field in the moving direction, which makes the train-induced wind field overlay with the crosswind field, producing the complex combined wind field. When the train runs at a constant speed, the combined wind field is stable. In the combined wind field, the combined wind velocity U_C depends on both the crosswind velocity and the train speed.

4.2.1 Influence of train speed on combined wind field

To investigate the influence of train speed on combined wind velocity, four train speeds of 200 km/h, 250 km/h, 300 km/h and 350 km/h are considered in the analysis, and the crosswind velocity is 20 m/s.

Illustrated in Fig. 12 are the distribution curves of the transverse components U_{CY} of the combined wind velocities with the height of monitoring points on the windward side (Y=-2.5 m, η_W =0.74) and the leeward side (Y=2.5 m, η_L =0.74). As shown in the figures, under different train speeds, the U_{CY} of monitoring points are all larger than the crosswind velocity 20 m/s, and they decrease with the

height. As can be seen from Fig. 12(a), under various train speeds, the U_{CY} on the windward side all appear at the height of train centroid
(ζ=0), and becomes smaller at the points whether higher or lower than the centroid. When train speed is 200 km/h, U_{CY} is the largest, because under higher train speeds, the train-induced wind flows faster, which is in the opposite direction against the crosswind, and thus blocks the flow stream.

As can be seen from Fig. 12(b), under various train speeds, the U_{CY} on the leeward side all reaches their maximums at the height of 1.5 m (ζ=0.41). When the train speed is 200 km/h, it reaches its peak of 35 m/s, which is much larger than that on the windward side. That is because the crosswind will accelerate after flowing around the car-body, so the wind velocity on the leeward side becomes larger than that on the windward side at the same height. As for the monitoring point 1b1 at the height of the train centroid (ζ=0), it is exactly located in the sheltered area of car-body, hence the transverse wind velocity is small.

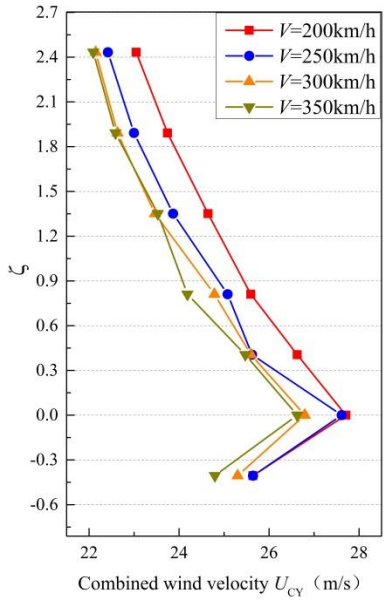

(a) windward side

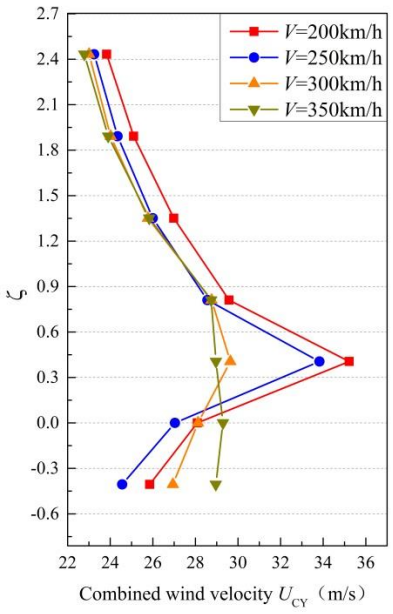

(b) leeward side

Fig. 12 Distributions of transverse components of combined wind velocities vs train speed

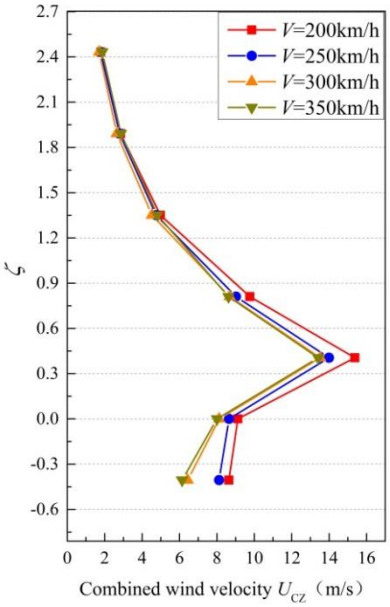

(a) windward side

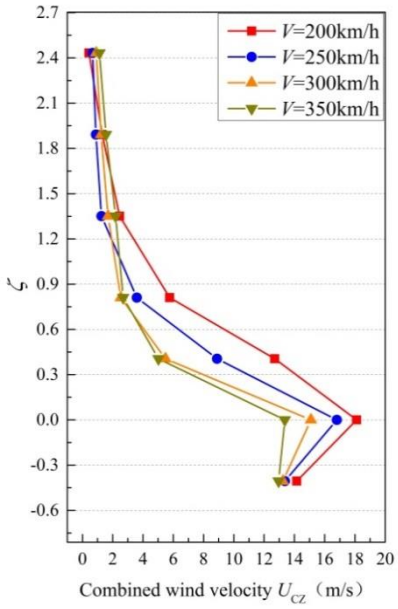

(b) leeward side

Fig. 13 Distributions of vertical components of combined wind velocities vs train speed

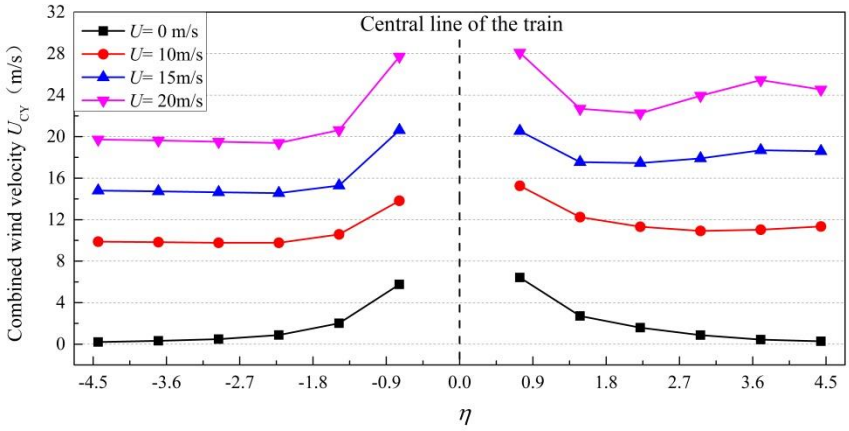

(a) U_{CY}

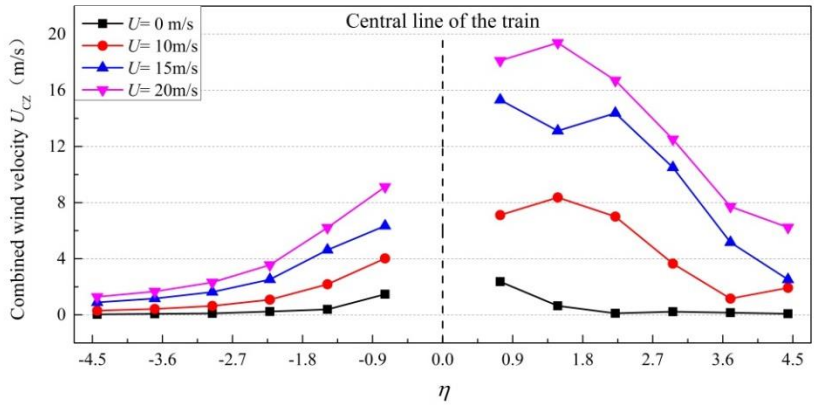

(b) U_{CZ}

Fig. 14 Transverse and vertical components of combined wind velocity on the windward side (left) and the leeward side (right)

Illustrated in Fig. 13 are the distribution curves of the vertical components U_{CZ} of the combined wind velocities with the height of monitoring points on both the windward side (Y=-2.5 m, η_w =0.74) and the leeward side (Y=2.5 m, η_L =0.74). As can be seen from Fig. 13(a), the U_{CZ} on the windward side changes slightly with train speed, and reaches its maximum at the train speed of 200 km/h, appearing at the height of 1.5 m (ζ=0.41), the level of the train roof. U_{CZ} decreases with the height above the train roof, from 15.4 m/s at the train roof to 2 m/s at the height of 9.0 m (ζ=2.43). As can be seen from Fig. 13(b), under different train speeds, the peak values of U_{CZ} on the leeward side all appear at the height of the train centroid (ζ=0). When the train speed is 200 km/h, U_{CZ} reaches 18.1 m/s, which is higher than that on the windward side.

4.2.2 Influence of crosswind velocity on combined wind field

When a train runs at a certain speed, the transverse component of combined wind velocity U_{CY} is mainly controlled by the crosswind. Considering train speed as 200 km/h and crosswind velocity as U=0 m/s, 10 m/s, 15 m/s and 20 m/s, four working conditions are analyzed. Fig. 14 shows the combined wind velocity at different monitoring points, where in the left part are the combined wind velocity curves on the windward side while in the right part are the curves on the leeward side.

As shown in Fig. 14(a), the transverse component U_{CY} of combined wind velocity increases with the crosswind velocity U. On the windward side, when the monitoring point is less than 10 m (η_w < 2.96) from the train centroid, the U_{CY} values are very close to the corresponding crosswind velocities, indicating the combined wind velocity is little affected by the train movement; For the monitoring point close to the train, U_{CY} increases rapidly. This is because that when the crosswind flows around the car-body, the 'climbing effect' occurs, which makes the combined wind velocity increase rapidly. Similar law can be observed on the leeward side, but when the distance to the train centroid is greater than 10 m (η_w>2.96), the train movement still has some effect on the combined wind velocity.

As shown in Fig. 14(b), the vertical component U_{CZ} of combined velocity also increases with the crosswind velocity. On both the windward side and the leeward side, U_{CZ} becomes greater when it gets closer to the train. On the leeward side, when crosswinds are 10 m/s, 15 m/s and 20 m/s, the U_{CZ} curves increase rapidly near the train body, and the peak values is almost twice of those on the windward side.

Table 2 Calculated maximum combined wind velocities and speed ratios

Train speed (km/h)	Windward 1a1 (Y=-2.5 m, Z=0 m)		Leeward 1b1 (Y=2.5m, Z=0 m)	
	U_{CY}（m/s）	C_V	U_{CY}（m/s）	C_V
200	27.71	3.85%	28.09	3.90%
250	27.62	3.07%	27.04	3.00%
300	26.80	2.48%	28.12	2.60%
350	26.63	2.11%	29.29	2.32%

To better analyze the influence of crosswind velocity and train speed on the combined wind velocity, the speed ratio C_v is used, which is defined as

$$C_v = \frac{U_{CY}(\text{m/s})}{V(\text{km/h})/3.6} \tag{6}$$

where: U_{CY} denotes the transverse component of combined wind velocity, and V is the train speed.

Table 2 shows the calculated results of maximum combined wind velocities and speed ratios at points 1a1 and 1b1 when the train runs on the bridge at speed of 200 km/h, 250 km/h, 300 km/h and 350 km/h under crosswind velocity of 20 m/s.

It is observed that on both the windward side and the leeward side, U_{CY} is mainly controlled by the crosswind but the speed ratio C_V decreases with the raise of train speed. In the train speed range of 200~350 km/h, C_v changes by 2%~4%. Because the faster the train speed, the bigger the 'push out' effect of train-induced wind field on the crosswind field, the maximum combined wind velocity at the windward monitoring point 1a1 decreases slightly when the train speed becomes higher. While on the leeward side, monitoring point 1b1 is located in the sheltered area of car-body, so when the crosswind flows around the car-body, many complicated vortexes are produced on the leeward side. These vortexes fall off and move with the time, which hence makes the U_{CY} of point 1b1 unstable at different train speeds.

4.3 Flow field analysis of combined wind field

In the combined wind field, there is an angle between the combined wind velocity and the train moving direction, so the maximum wind pressure on the headstock surface does not exactly appear on the nose, but relates to the relative magnitudes of train speed and crosswind velocity. Herein, four cases of crosswind velocities of 0 m/s, 10 m/s, 15 m/s and 20 m/s are considered, to analyze the wind pressure distribution on the car-body surface under train speed of 200 km/h. Shown in Figs. 15(a)-15(d) are the surface pressure nephograms of the train under different crosswind velocities.

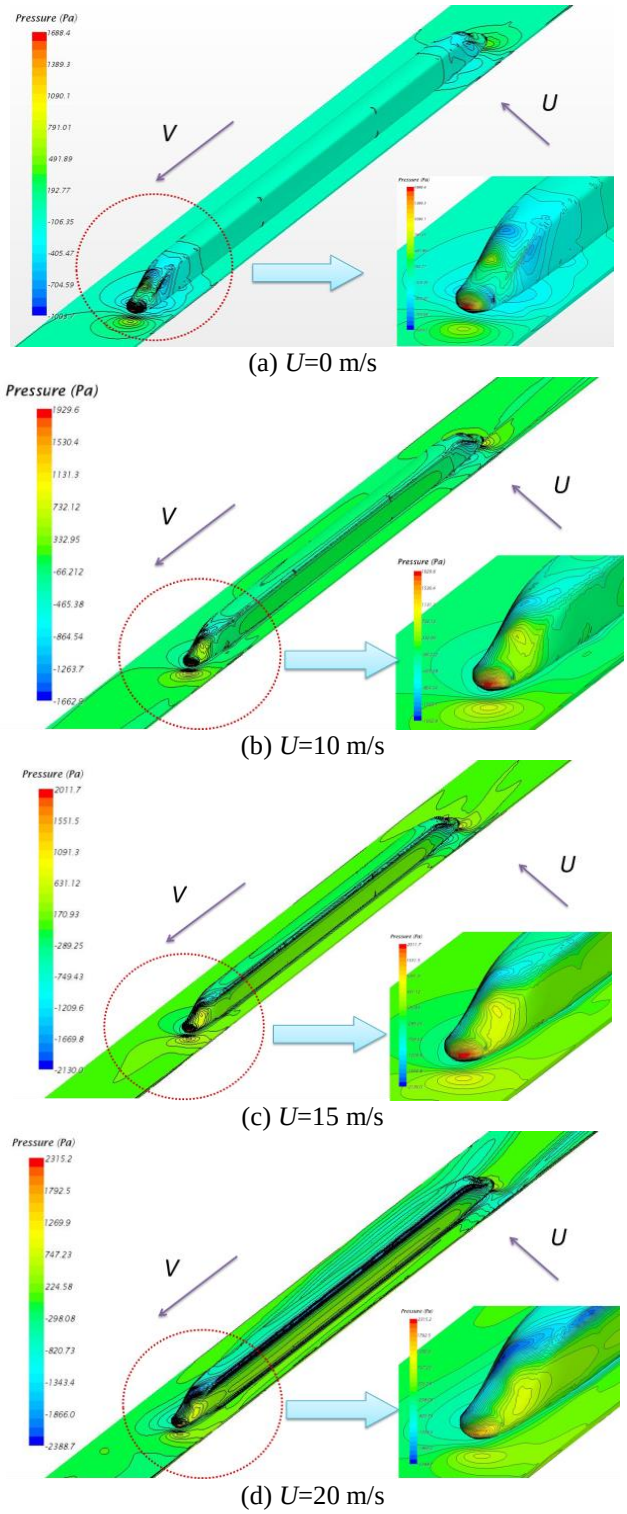

(a) U=0 m/s

(b) U=10 m/s

(c) U=15 m/s

(d) U=20 m/s

Fig. 15 Pressure nephograms of wind field at different crosswind velocities (train speed V=200 km/h)

As can be seen from the figures, the train-induced wind mainly affects the pressure distributions at the head surface and the tail surface of the train. On the headstock nose, there exists a positive pressure zone, which extends outward in a circular form. As shown in Fig. 15(a), the pressure at the headstock nose is the biggest, which is symmetrically

distributed about the vertical longitudinal section (section XOZ) of the train. Under crosswind, this positive pressure zone moves with the increase of crosswind velocity from the nose to the windward side of the car-body, and the pressure value also increases. In addition, there is another positive pressure zone on the top of the headstock, and the pressure at the zone center is the biggest. Similarly, this positive pressure zone also moves with the increase of crosswind velocity. As shown in Fig. 15(d), when the crosswind velocity is increased to 20 m/s, the center of positive pressure zone on the top of headstock has moved to the windward side of the train. On the contrary, the leeward side of headstock is the negative pressure zone, which gradually moves to the car-roof with the increase of crosswind velocity.

4.4 Comparison of train-induced wind fields produced by two modeling methods

Train movement can also be simulated by the static train model based on the theory of relatively movement, in which the train is static while the ground moves with a speed of the train in opposite direction (-*V*). In order to simulate the relative motion, a moving wall boundary with the same speed as the inlet flow is applied in the numerical calculation.

Taking the condition of train speed 200 km/h and non-crosswind as an example, the train-induced wind field is produced by both the static train model and the moving train model, respectively, to compare the train-induced wind fields produced by the two methods. Fig. 16 shows the distribution of transverse components U_{TY} of train-induced wind velocity at the height of train centroid versus the distance to the train.

As can be seen from Fig. 16, when the transverse distance of monitoring point to the train is more than 5 m (η_w >1.48), the difference between the calculated results by the two methods is small. At the distance of 2.5 m (η_w =0.74), the amplification ratio is the maximum, which is 4.62, corresponding to U_{TY}=5.75 m/s of the moving train model and U_{TY}=1.25 m/s of the static train model.

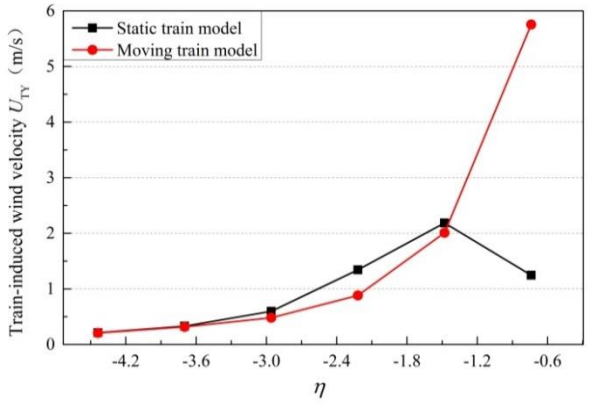

Fig. 16 Distribution of U_{TY} calculated by static train model and moving train model

Along with the decrease of the transverse distance, the U_{TY} calculated by the static model gets smaller while that by the moving train model becomes bigger. That is because in the static train model, the flow is an active movement, which is impaired when meeting the car-body, leading to a smaller wind velocity near the car-body; while in the moving train model, the flow is a passive movement, which is driven by the train movement, leading to a severer air flow near the car-body. This comparison illustrates that using the static train model and the theory of relative movement cannot get the real flow field around the car-body, instead, the moving train model is more applicable in analyzing the train induced wind field.

5. Conclusions

When a train runs on the bridge, the train-induced wind combines with the crosswind to form a complicated combined wind field, which varies with train speed and crosswind velocity. In this paper, the train-induced wind fields with and without crosswind are analyzed by establishing the train model. The main conclusions are as follows:

• Without influence of crosswind, the train-induced wind velocity increases with the train speed, but decreases with the distance from the train. When the distance is greater than 10 m (η_w>2.96), the train-induced wind velocity can be neglected. Among the monitoring point column -1a1~-6a1 (η_w =0.74, ζ=-0.41~2.43), the maximum wave peak is 168 Pa and the maximum wave trough is -150 Pa.

• Under crosswind, the combined wind velocity is mainly controlled by the crosswind and also increases with the train speed. Under various train speeds, the U_{CY} on the windward side all appear at the height of train centroid (ζ =0). The main influence scope of train-induced wind field is within 7 m (η_w ≤1.89). When the distance from the train is greater than 7 m (η_w >1.89, the train-induced wind velocity can be neglected.

• Under crosswind, the transverse components of combined wind velocity on the windward side and the leeward side of the train are basically same, but the vertical component on the leeward side is bigger than that on the windward side. On the windward side, when the distance is more than 10 m (η_w <2.96) from the train centroid, the U_{CY} values are very close to the corresponding crosswind velocities. In the train speed range of 200~350 km/h, C_v changes between 2%~4%.

• In the combined wind field, the combined wind velocity has a certain angle with the train moving direction. With the increase of crosswind velocity, the peak pressure point on the headstock moves from the nose to the windward side, and the pressure on the car-body also increases.

• Adopting static train model and the theory of relative movement cannot get the real flow field around the car-body. At the distance of 2.5 m (η_w =0.74), the amplification ratio is the maximum, which is 4.62, corresponding to U_{TY}=5.75 m/s of the moving train model and U_{TY}=1.25 m/s of the static train model.

Acknowledgements

This work was supported by the National Natural Science Foundations (U1434205, 51720105005 and 51508018) and the National Basic Research Program ("973" Program) (Grant No. 2013CB036203) of China.

References

Ahmed, S.R., Gawthorpe, R.G. and Mackrodt, P.A. (1985), "Aerodynamics of road and rail vehicles", *Vehicle. Syst. Dyn*, **14**(4-6), 319-392.

Asress, M.B. and Svorcan, J. (2014), "Numerical investigation on the aerodynamic characteristics of high-speed train under turbulent crosswind", *J. Mod Transp*, **22**(4), 225-234.

Avadiar, T., Bell, J., Burton, D., Cormaty, H. and Li, C. (2016), "Analysis of high-speed train flow structures under crosswind", *J. Mech. Sci. Technol*., **30**(9), 3985-3991.

Baker, C.J. (2002), The wind tunnel determination of crosswind forces and moments on a high speed train (Springer Berlin Heidelberg, 2002), 46-60.

Cai, C.S., Hu, J.X., Chen, S.R., Han, Y., Zhang, W. and Kong, X. (2015), "A coupled wind-vehicle-bridge system and its applications: A review", *Wind Struct.*, **20**(2), 117-142.

Chen, Z.W., Xu, Y.L., Li, Q. and Wu, D.J. (2011), "Dynamic stress analysis of long suspension bridges under wind, railway, and highway loadings", *J. Bridge Eng .- ASCE*, **16**(3), 383-391.

Guo, W., Xia, H., Karoumi, R., Zhang, T. and Li, X. (2015), "Aerodynamic effect of wind barriers and running safety of trains on high-speed railway bridges under cross winds", *Wind Struct*., **20**(2), 213-236.

Guo, W.W., Xu, Y.L., Xia, H., Zhang, W.S. and Shum, K.M. (2007), "Dynamic response of suspension bridge to typhoon and trains. Ii: numerical results", *J. Struct*., **133**(1), 12-21.

Hemida, H., Baker, C. and Gao, G. (2014), "The calculation of train slipstreams using large-eddy simulation", *Proceedings of the Institution of Mechanical Engineers Part F-Journal of Rail and Rapid Transit*, **228**(1), 25-36.

Huang, S., Hemida, H. and Yang, M.Z. (2016), "Numerical Calculation of the Slipstream Generated by a Crh2 High-Speed Train", *Proceedings of the Institution of Mechanical Engineers Part F-Journal of Rail and Rapid Transit*, **230**(1), 103-116.

Krajnovic, S., Ringqvist, P., Nakade, K. and Basara, B. (2012), "Large eddy simulation of the flow around a simplified train moving through a crosswind flow", *J. Wind Eng. Ind. Aerod.*, **110**, 86-99.

Li, Y., Hu, P., Xu, Y.-L., Zhang, M. and Liao, H. (2014), "Wind loads on a moving vehicle-bridge deck system by wind-tunnel model test", *Wind Struct.*, **19**(2), 145-167.

Premoli, A., Rocchi, D., Schito, P. and Tomasini, G. (2016), "Comparison between steady and moving railway vehicles subjected to crosswind by Cfd analysis", *J. Wind Eng. Ind. Aerod.*, **156,** 29-40.

Rezvani, M.A. and Mohebbi, M. (2014), "Numerical calculations of aerodynamic performance for atm train at crosswind conditions", *Wind Struct.*, **18**(5), 529-548.

Wang, B., Xu, Y.L. and Li, Y.L. (2015), "Dynamic analysis of wind-vehicle-bridge systems using mutually-affected aerodynamic parameters", *Wind Struct.*, **20**(2), 191-211.

Xu, Y.L., Guo, W.W., Chen, J., Shum, K.M. and Xia, H. (2007), "Dynamic response of suspension bridge to typhoon and trains. I: field measurement results", *J. Struct.*, **133**(1), 3-11.

Yao, S.B., Sun, Z.X., Guo, D.L., Chen, D.W. and Yang, G.W. (2013), "Numerical study on wake characteristics of high-Speed trains", *Acta Mech. Sinica*, **29**(6), 811-822.

Zhai, W.M., Yang, J.Z., Li, Z. and Han, H.Y. (2015), "Dynamics of high-speed train in crosswinds based on an air-train-track interaction model", *Wind Struct.*, **20**(2), 143-168.

Zhang, N., Ge, G.H., Xia, H. and Li, X.Z. (2015), "Dynamic analysis of coupled wind-train-bridge system considering tower shielding and triangular wind barriers", *Wind Struct.*, **21**(3), 311-329.

Zhang, T., Xia, H. and Guo, W.W. (2013), "Analysis on running safety of train on bridge with wind barriers subjected to cross wind", *Wind Struct.*, **17**(2), 203-225.

CC